crystals

MDPI

Article

Radiation-Induced Disorder and Lattice Relaxation in $Gd_3Ga_5O_{12}$ Under Swift Xe Ion Irradiation

Zhakyp T. Karipbayev [1], Gulnara M. Aralbayeva [1,*], Abil T. Zhalgas [1], Kymbat Burkanova [1], Amangeldy M. Zhunusbekov [1], Ilze Manika [2], Abdirash Akilbekov [1], Aizat Bakytkyzy [1], Sergii Ubizskii [3], Gibrat E. Sagyndykova [1], Marina Konuhova [2], Anatolijs Sarakovskis [2], Yevheniia Smortsova [4] and Anatoli I. Popov [1,2,*]

[1] Department of Technical Physics, Institute of Physics and Technology, L.N. Gumilyov Eurasian National University, Satpayev Street 2, Astana 010008, Kazakhstan; karipbayev_zht_1@enu.kz (Z.T.K.); abil_zht_1@enu.kz (A.T.Z.); kymbatburkan@gmail.com (K.B.); zhunusbekov_am@enu.kz (A.M.Z.); akilbekov_at@enu.kz (A.A.); aizat.bakytkyzy.1@gmail.com (A.B.); sagyndykova_gye@enu.kz (G.E.S.)

[2] Institute of Solid State Physics, University of Latvia, Kengaraga 8, Street, LV-1063 Riga, Latvia; ilze.manika@cfi.lu.lv (I.M.); marina.konuhova@cfi.lu.lv (M.K.); anatolijs.sarakovskis@cfi.lu.lv (A.S.)

[3] Semiconductor Electronics Department, Lviv Polytechnic National University, S. Bandera Street 12, 79013 Lviv, Ukraine; sergii.b.ubizskii@lpnu.ua

[4] Deutsches Elektronen-Synchrotron (DESY), 22603 Hamburg, Germany; yevheniia.smortsova@desy.de

* Correspondence: aralbayeva_gm_1@enu.kz (G.M.A.); popov@latnet.lv (A.I.P.)

Abstract

This study presents a comprehensive Raman spectroscopic and mechanical investigation of $Gd_3Ga_5O_{12}$ (GGG) single crystals irradiated with 231 MeV ^{131}Xe ions at fluences ranging from 1×10^{11} to 3.3×10^{13} ions/cm^2. Raman analysis reveals that all fundamental vibrational modes of the garnet structure remain observable up to the highest fluence, with the preservation of garnet crystalline topology/absence of secondary crystalline phases. However, significant line broadening (FWHM increase by 20–100%) and low-frequency shifts indicate progressive lattice disorder and phonon-defect scattering. High-frequency Ga-O stretching modes (A_{1g}, T_{2g} ~740 cm^{-1}) remain the most resistant to irradiation, while low-energy translational modes involving Gd^{3+} ions exhibit pronounced degradation and partial disappearance at high fluence. Complementary nanoindentation measurements show radiation-induced softening: hardness decreases by up to ≈60% at 3.3×10^{13} ions/cm^2, consistent with amorphization and overlapping ion tracks (~10–12 μm deep). Raman spectroscopy shows that the garnet lattice remains as the only crystalline phase up to 3.3×10^{13} ions/cm^2, while significant line broadening, mode suppression and a strong hardness decrease indicate progressive structural disorder and partial amorphization of the near-surface region. These results demonstrate that GGG maintains crystalline integrity below the track-overlap threshold (~6 keV/nm) but undergoes strong structural relaxation and mechanical weakening once this limit is exceeded. A new analytical methodology has been developed to quantify radiation-induced structural degradation.

Keywords: $Gd_3Ga_5O_{12}$ single crystals; Raman spectra; optical absorbance; nanoindentation; radiation-induced defects; scintillation materials

Academic Editors: Daisuke Nakauchi and Weichao Bao

Received: 23 October 2025
Revised: 11 December 2025
Accepted: 17 December 2025
Published: 18 December 2025

Citation: Karipbayev, Z.T.; Aralbayeva, G.M.; Zhalgas, A.T.; Burkanova, K.; Zhunusbekov, A.M.; Manika, I.; Akilbekov, A.; Bakytkyzy, A.; Ubizskii, S.; Sagyndykova, G.E.; et al. Radiation-Induced Disorder and Lattice Relaxation in $Gd_3Ga_5O_{12}$ Under Swift Xe Ion Irradiation. *Crystals* **2025**, *15*, 1065. https://doi.org/10.3390/cryst15121065

1. Introduction

Gadolinium gallium garnet (GGG, $Gd_3Ga_5O_{12}$) is a versatile platform for photonics. Upon doping with rare-earth ions (Ce^{3+}, Er^{3+}, Dy^{3+}, Sm^{3+}, Nd^{3+}, Eu^{3+}), it operates as a phosphor, laser, and scintillation material [1–10]. In particular, Ce:GGG ex-

hibits intense 4f-5d transitions suitable for phosphor and scintillation applications [1–3], Bi^{3+}/Eu^{3+} co-modifications function as UV→VIS converters [9], and Er^{3+}/Pr^{3+}, Dy^{3+}, Sm^{3+}, and Nd^{3+} provide laser-active transitions spanning from the orange-red to the near-IR spectral regions [4–6,8–10]. Transition-metal doping (e.g., Cr^{3+}) enables tuning of the crystal field and energy-transfer pathways, broadening the spectral engineerability of active media and phosphors [11]. For substrate applications, GGG is grown as an epitaxial wafer from "pure" polycrystalline feedstock [12]; mechanical-technological protocols (nanoscratch testing, crack-free grinding, nanoindentation) deliver optically smooth surfaces and low loss [13–15].

GGG crystallizes in the cubic garnet structure (Ia-3d) with a GaO_4/GaO_6 framework and dodecahedrally coordinated Gd^{3+}. Isomorphic substitutions by $Ca^{2+}/Mg^{2+}/Zr^{4+}$ finely tune the lattice parameter, defectiveness, and dislocation density; Rietveld refinements correlate with shifts/broadening of Raman modes ($A_{1g}/E_g/T_{2g}$), making Raman spectroscopy a convenient rapid indicator of microstructural changes [16]. In $Y_3Fe_5O_{12}$(YIG)/GGG heterosystems, Raman signatures are sensitive to interfacial stresses and reaction-diffusion processes at LPE interfaces [17], while remote epitaxy through graphene confirms the suitability of GGG as a platform for transferable thin films [18]. Brillouin spectroscopy in multilayer YIG/GGG structures highlights the linkage between magnoacoustics and mechanically induced stress governed by substrate quality [19]. Hydrostatic pressure induces polyhedral distortions and frequency shifts/broadening (FWHM—full width at half maximum) of Raman lines [20]; similar trends reported for related garnets ($Lu_3Ga_5O_{12}$) aid calibration of deformation-induced effects in GGG [21]. Impurity diffusion (e.g., Co) underscores the role of thermal treatment and defect chemistry in forming traps/color centers [22]. Cation substitutions (e.g., Al) illustrate the controllability of GGG crystal chemistry and associated structure-property couplings in garnets [23].

Two limiting radiation-damage scenarios are observed in GGG. (i) Neutron irradiation predominantly generates Frenkel point defects and their clusters, leading to a moderate increase in induced absorption and Raman-diagnosable microimperfections (mode shifts, FWHM growth, elevated background scattering) without loss of long-range order [24]. (ii) Swift heavy ions (U, Kr, etc.) with high electronic stopping (S_e) produce latent tracks with local amorphization and elastic-stress fields, thereby enhancing optical losses and yielding a pronounced Raman signature of disorder [25–29]. The measured track cross-sections and their scale are well described by the inelastic thermal spike model (ITSM), defining thresholds for track formation and conditions for subsequent recrystallization [28–33]; at the macroscopic level, out-of-plane swelling is recorded as an integral marker of bulk defect accumulation [29]. At large S_e, electronic sputtering is also observed, with yields and stoichiometric shifts correlating with track physics and local lattice degradation [30].

From an optical standpoint, radiation-induced absorption arises from contributions of color centers and Urbach-tail broadening. Under neutron exposure, optical absorption increases persistently in the UV/visible range, in concert with Raman line broadening and background growth [24]. In the case of ^{84}Kr ion irradiation, correlated changes in optical, structural, and mechanical metrics indicate a transition from defect-modulated quasi-crystalline states to local amorphization within tracks as S_e and/or fluence increase [27]. Comparative studies across garnets (including YIG as a model) reveal a common set of spectral damage signatures and amorphization → recrystallization pathways upon annealing [31,32]; consistency of mechanisms is further supported by XRD/AFM data for YAG under swift ions [33,34] and cross-publication verification for YIG [35]. Notably, even without ion bombardment, color centers can emerge in doped GGG/YAG, establishing a "background" of defect chemistry for radiation testing [36].

Raman metrics of dose accumulation include: (i) $\Delta\omega$—frequency shifts in GaO_4/GaO_6 framework modes; (ii) ΔFWHM—line broadening as an indicator of microimperfections and phonon-defect scattering; (iii) $I_{disorder}/I_{ref}$—mode-to-background intensity ratios sensitive to local amorphization [24,28,32]. A useful "calibration" is provided by pressure analogies, where directed shifts/broadening reflect polyhedral distortions [20,21]. In multilayer YIG/GGG, dose-dependent Raman changes are compounded by interfacial effects (stress, reaction-diffusion), which are critical for the stability of spin-wave and magnoacoustic regimes; here Raman naturally complements Brillouin spectroscopy as a stress- and defect-sensitive technique [19,31].

A radiation-hardness strategy for the GGG platform follows: control of oxygen stoichiometry and defect chemistry during growth, minimization of dislocations and subsurface damage, optimization of isomorphic substitutions (Ca/Mg/Zr) for stress relaxation, management of extrinsic-ion diffusion (Co), and interfacial quality; a defined post-irradiation annealing protocol—under continuous monitoring by optical (band-edge/induced absorption) and Raman metrics ($\Delta\omega$, ΔFWHM, background) [16,19,24,27–36].

Recent studies on radiation effects in oxides and fluorides have provided a broader framework for understanding defect formation in complex garnets. In ZrO_2 and MgO ceramics, nanostructuring and irradiation temperature were shown to control polymorphic stability, defect clustering, and resistance to amorphization [37–39]. For BeO, diffusion of vacancy-type defects and relaxation of residual stress were identified as key factors governing swelling and microstructural expansion [40]. Investigations of LiF crystals under electron and heavy-ion irradiation revealed correlations between color-center stability and thermal annealing behavior [41–43]. Swift heavy ion studies on $Y_3A_5O_{12}$ and $Y_3Fe_5O_{12}$ garnets demonstrated track formation, amorphization-recrystallization transitions, and stress-induced softening [30,44–47]. Complementary diffraction modeling of Nd:YAG ceramics confirmed defect-assisted strain relaxation [48]. Together, these findings emphasize the relevance of comparing radiation-induced disorder and phenomenological interpretation consistent with partial saturation of defect accumulation in $Gd_3Ga_5O_{12}$ with that in structurally related oxides and halides.

In the present study, we analyze changes in the Raman spectra of GGG induced by ^{131}Xe heavy ions with an energy of 231 MeV at fluences of 10^{11}, 10^{12}, 10^{13}, and 3.3×10^{13} ions/cm^2. Particular attention is paid to frequency shifts and linewidth broadening (without considering intensity changes), assessing the resilience of different vibrational modes to radiation exposure, and correlating the observed modes with specific structural fragment vibrations (Ga-O bonds in tetrahedral and octahedral units, vibrations involving Gd^{3+}). Additionally, changes in the microhardness of irradiated crystals are examined defect accumulation and degradation of mechanical properties.

2. Materials and Methods

Single crystals of GGG were grown using the Czochralski technique from an iridium crucible under a mildly oxidizing atmosphere at the Scientific Research Company "Electron-Carat" (Lviv, Ukraine). The growth environment comprised a controlled mixture of 98% argon and 2% oxygen. High-purity Gd_2O_3 and Ga_2O_3 powders (99.99 wt%) were employed as starting materials. Since tetravalent impurity ions such as Si^{4+} and Zr^{4+} in the raw oxides can induce cation vacancies and promote spiral growth in rare-earth gallium garnets, a small amount of CaO (10^{-2}–10^{-3} wt%) was added to the melt to mitigate these undesirable effects. The pristine $Gd_3Ga_5O_{12}$ single crystals crystallize in the cubic garnet structure (space group $Ia\bar{3}d$) with a lattice parameter $a \approx 12.368$ Å. The high structural quality and absence of secondary phases were verified by X-ray diffraction, as reported previously [27].

The GGG single crystal samples were irradiated along the ⟨111⟩ direction with ^{131}Xe ions at an energy of 231 MeV and at various fluences of 10^{11}, 10^{12}, 1×10^{13} and 3.3×10^{14}, ion/cm^2. The ion beam current was in the range of 25–30 nA/cm^2. The samples irradiated with high-energy xenon ions showed no visible damage. The irradiation was carried out using the DC-60 heavy-ion accelerator at the Institute of Nuclear Physics in Astana, Kazakhstan.

Optical absorption spectra were recorded at room temperature using an PERSEE T8DCS spectrophotometer (Beijing Purkinje General Instrument Co., Ltd., Beijing, China) in the wavelength range of 200–800 nm with a spectral resolution of 1.0 nm.

The micro- and nanomechanical properties of the samples were investigated using an Agilent Nano G200 nanoindenter (Santa Clara, CA, USA), enabling continuous stiffness measurements (CSM) through simultaneous recording of applied load and corresponding indenter displacement. Measurements were performed both on the irradiated surface and along cross-sectional profiles obtained by cleaving the irradiated samples along the ion beam direction. Surface profile measurements provided more informative data, allowing evaluation of structural and mechanical property variations along the entire ion penetration path and their dependence on depth, defined as the distance from the irradiated surface. The nanoindentation system was calibrated prior to measurements using reference materials with well-established mechanical properties. A fused silica standard ($E \approx 72$ GPa, $\nu = 0.17$) was employed for calibration of the indenter area function and frame compliance. The calibration procedure was repeated periodically to ensure reproducibility and stability of the measured hardness and elastic modulus values.

In CSM mode, hardness and Young's modulus were determined as functions of penetration depth. Calibration was performed using certified reference samples following the procedures recommended by the manufacturer. For each measurement point, ten indentations were performed, and the mean values were calculated to ensure accuracy and reproducibility.

Raman spectroscopy measurements were performed on the (111) surface of the GGG crystal. Raman spectra were acquired using a TriVista CRS Raman spectrometer (Princeton Instruments, Trenton, NJ, USA) equipped with a triple monochromator and a cooled CCD detector, providing a spectral resolution better than 0.1 cm^{-1}. Excitation was achieved with a 532 nm solid-state laser (3.63 mW) laser at room temperature (RT), selected for its high stability and strong resonance with characteristic vibrational modes of the studied material. The scattered radiation was collected in a backscattering geometry using a confocal optical microscope with submicron spatial resolution, allowing precise localization of the probed area on the sample surface. The laser power at the sample was carefully adjusted to avoid local heating or damage. The spectrometer was calibrated using the 520.7 cm^{-1} line of a crystalline silicon standard. All measurements were conducted at room temperature, and the acquired spectra were corrected for background and instrument response. The micro-Raman spectra were recorded as averages of measurements performed at five different positions on the crystal surface using a probing laser spot with a diameter of approximately 1 μm, in order to minimize the influence of local inhomogeneity effects. While this averaging improves the overall reproducibility of the Raman response, it also introduces cumulative uncertainties in the absolute Raman intensity due to unavoidable variations in local focusing conditions, surface morphology, and scattering geometry at different measurement points. For this reason, the absolute Raman intensity was not considered a sufficiently reliable quantitative parameter and was not used for disorder analysis. At the excitation wavelength of 532 nm, GGG is essentially transparent due to its wide band gap, resulting in a large optical penetration depth. Under confocal micro-Raman conditions, the effective probing depth is therefore governed by the confocal

geometry rather than by optical absorption and is estimated to be on the order of 1–3 μm. Consequently, the recorded Raman signal represents an average response from a near-surface volume encompassing both amorphous ion-track regions and the surrounding defect-rich crystalline matrix. For each measurement, the acquisition time was 20 s per accumulation, and each spectrum represents the sum of five consecutive accumulations (co-addition), resulting in an effective integration time of 100 s. The micro-Raman spectra were recorded as averages over five different positions on the crystal surface using a laser spot with a diameter of approximately 1 μm in order to minimize the influence of local inhomogeneities.

3. Results and Discussion

3.1. Optical Absorption Spectra

Figure 1a presents the optical absorption spectra of GGG single crystals irradiated with 231 MeV ^{131}Xe ions at various fluences. The pristine crystal exhibits a sharp fundamental absorption edge in the ultraviolet (UV) region, followed by transparency in the visible range. With increasing irradiation fluence, the absorption edge gradually shifts to longer wavelengths, reflecting radiation-induced modifications in the electronic structure of the crystal. At low fluences (10^{11}–10^{12} ions/cm^2), this effect is weak, whereas at 10^{13} and especially 3.3 × 10^{13} ions/cm^2, significant edge broadening and visible transparency reduction are observed, indicating defect accumulation and the formation of additional absorption centers related to point defects and ion tracks.

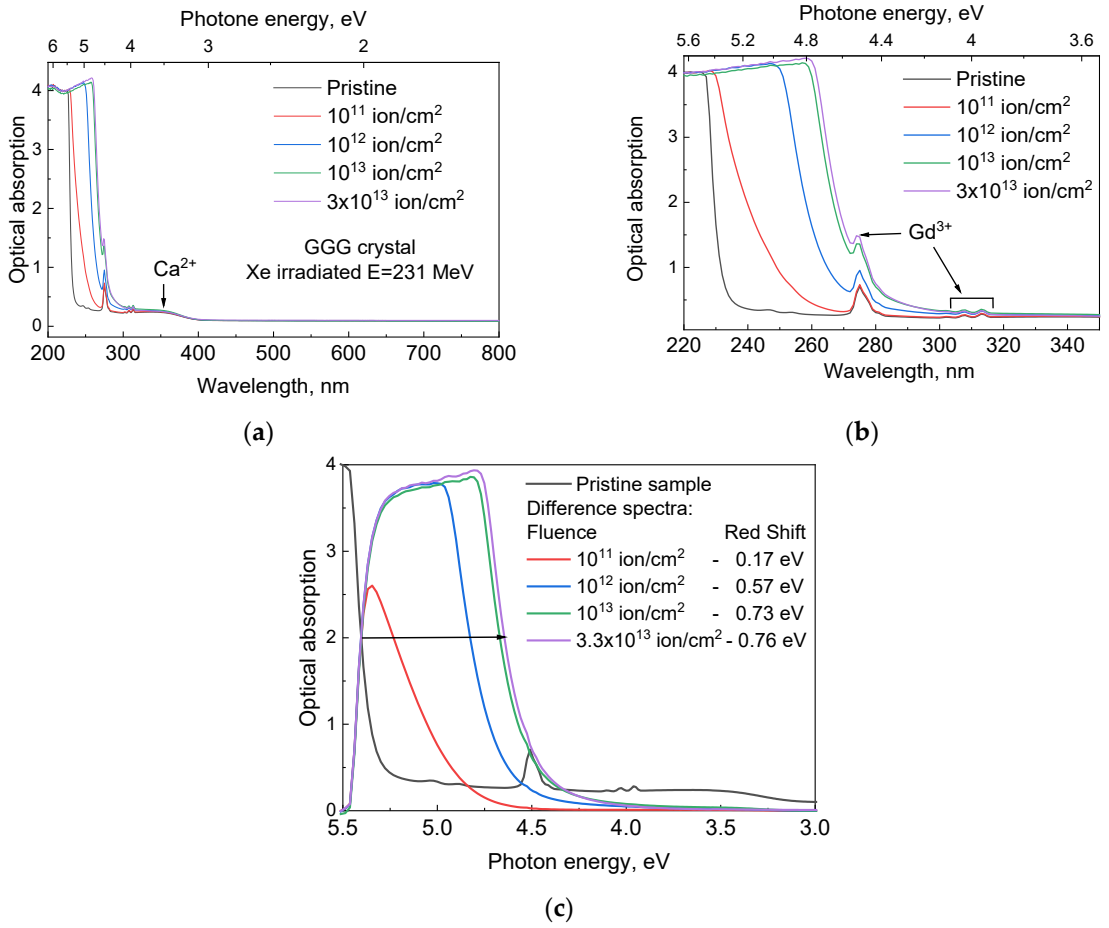

Figure 1. Absorption spectra of GGG single crystals: Pristine and ^{131}Xe ion-irradiated with E = 231 MeV by various fluence (**a**), zoomed at 220–350 nm (**b**) and difference spectra (**c**).

The visible absorption bands at 254, 275, and 313 nm are attributed to the electronic transitions $^8S_{7/2} \rightarrow {}^6D_j$, $^8S_{7/2} \rightarrow {}^6I_j$, and $^8S_{7/2} \rightarrow {}^6P_j$, respectively. Impurity dopants may introduce additional energy levels; for instance, the presence of small amounts of Ca^{2+} creates oxygen vacancies, which manifest as an additional absorption band near 350 nm [24]. It should be emphasized that ^{131}Xe-ion irradiation does not introduce additional Ca-related defects into the GGG lattice. While swift heavy-ion irradiation may generate additional point defects, it does not selectively enhance the accumulation of $Ca–V_O$ complexes. Within the considered fluence range, the overall shape and energy position of the 350 nm absorption band remain essentially unchanged, indicating that irradiation primarily modifies the local structural disorder rather than the concentration of the Ca-stabilized vacancy centers themselves. Therefore, the evolution of the 350 nm band should be regarded as weakly sensitive to ^{131}Xe fluence and mainly reflecting the pre-existing defect subsystem.

Figure 1b shows differential spectra obtained by subtracting the spectrum of the unirradiated sample from those of the irradiated crystals. This approach allows a clear observation of the absorption edge shift at a fixed optical density (approximately 2). The graph indicates that the magnitude of the shift increases from 0.17 eV at low fluences to 0.76 eV at the maximum irradiation dose. This effect is attributed to ion-induced absorption arising from defect states formed near the band edge. ^{131}Xe ion irradiation leads to additional absorption and a significant redshift of the absorption edge. A pronounced dependence of the edge shift on fluence is observed: higher doses result in stronger ion-induced absorption.

3.2. Raman Spectroscopy

3.2.1. Raman Spectra

Pristine GGG exhibits sharp Raman lines in the ~100–800 cm^{-1} range, corresponding to first-order lattice vibrations of the garnet structure, reflecting a high degree of long-range crystalline order. Figure 2 presents representative Raman spectra (λ_{exc} = 532 nm) of the pristine and ^{131}Xe-irradiated crystals, revealing a systematic evolution of the vibrational response with increasing fluence of 231 MeV ions. After irradiation, the majority of Raman modes decrease in intensity and broaden, reflecting progressive disordering of the crystal lattice, partially overlap, while remaining clearly identifiable even at the maximum fluence of 3.3×10^{13} ions/cm^2, which indicates that the average garnet topology is preserved and that complete amorphization does not occur. At the same time, no new sharp Raman lines emerge across the studied spectral range, excluding the formation of secondary crystalline phases and confirming that irradiation induces structural disorder within the original garnet lattice rather than a phase transformation. A pronounced feature accompanying irradiation is the monotonic rise in a broad background signal, particularly evident in the high-frequency region above ~1000–2000 cm^{-1}, where the pristine crystal shows minimal intensity. This elevated background is characteristic of enhanced scattering from highly distorted or locally amorphized regions created along swift heavy-ion tracks and their overlap at higher fluences. The combined presence of preserved but broadened phonon modes and an increasing continuum background demonstrates that ^{131}Xe irradiation leads to the gradual accumulation of radiation-induced disorder and the emergence of locally disordered or quasi-amorphous zones embedded in a predominantly crystalline matrix. This interpretation is fully consistent with X-ray diffraction results, which show only lattice deformation and a reduction in the coherence length without the appearance of new phases even at the highest fluences [24], corroborating the conclusion that the observed spectral changes arise from partial, track-related disordering rather than macroscopic amorphization of GGG.

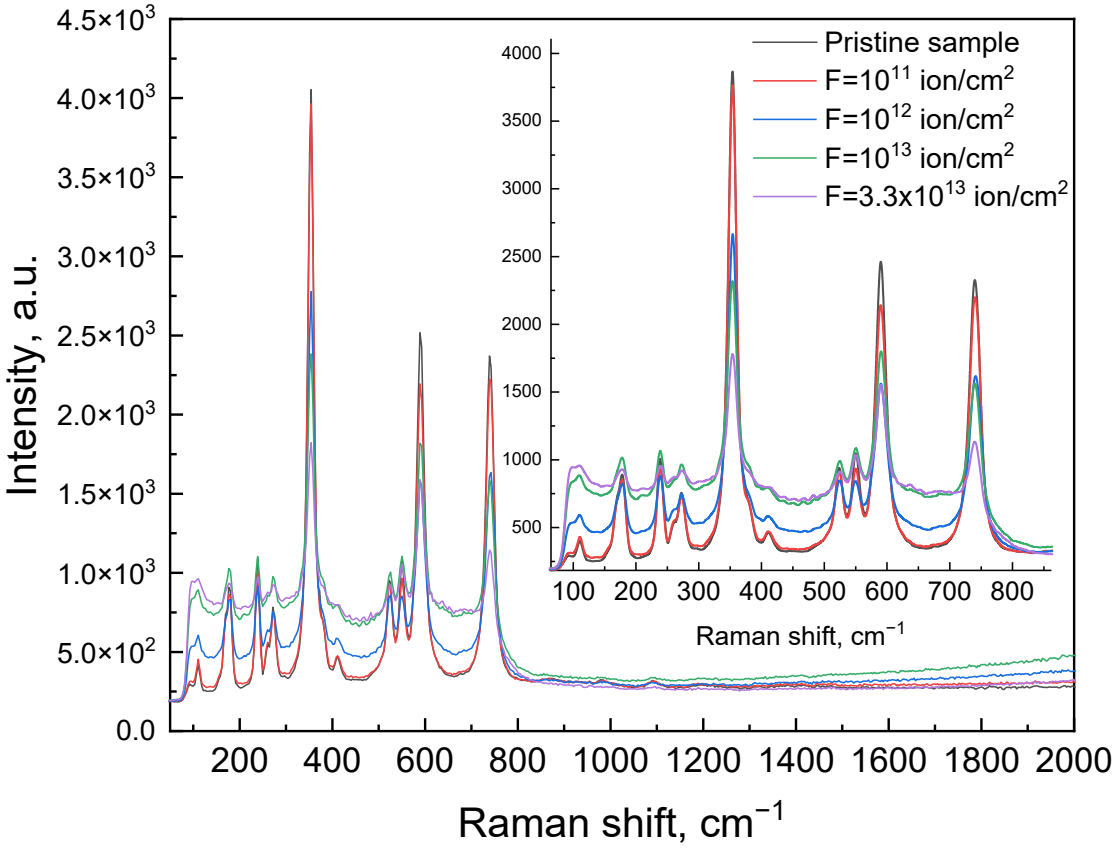

Figure 2. Baseline corrected Raman spectra of GGG single crystals: Pristine and ^{131}Xe ion-irradiated with E = 231 MeV by various fluences.

Under swift heavy-ion irradiation, the damaged material can be described as consisting of amorphous ion-track cores (region (a)) embedded in a crystalline matrix (region (b)) that progressively accumulates point defects and strain. The irradiation-induced evolution of Raman peak intensity does not originate from a single structural region. Instead, the measured Raman signal reflects the combined contributions of the amorphous track cores, which suppress discrete phonon modes, and the defect-rich crystalline matrix, where strain and point defects reduce the Raman cross section and phonon coherence. Consequently, the decrease in Raman peak intensity cannot be interpreted as a measure of the undamaged matrix fraction alone, but rather as an effective indicator of overall structural disorder. This interpretation is consistent with the observed deviation from a simple Poisson-law behavior of the Raman intensity with fluence.

3.2.2. FWHM of Raman Spectra

For a more detailed analysis of the Raman spectra, a baseline correction was applied to remove the background contribution associated with fluorescence and nonresonant scattering, thereby isolating the intrinsic vibrational features of the material (Figure 3a). Overall, with increasing fluence, the Raman spectra show progressive degradation of the coherent vibrational structure: at 10^{11} ions/cm^2, changes are minimal, whereas at 10^{13}–3.3×10^{13} ions/cm^2, peaks broaden and merge, and their contrast against the background decreases. At the highest fluences, the vibrational spectrum approaches that of an amorphous state, with broad smoothed bands reflecting the phonon density of states of a disordered lattice [26].

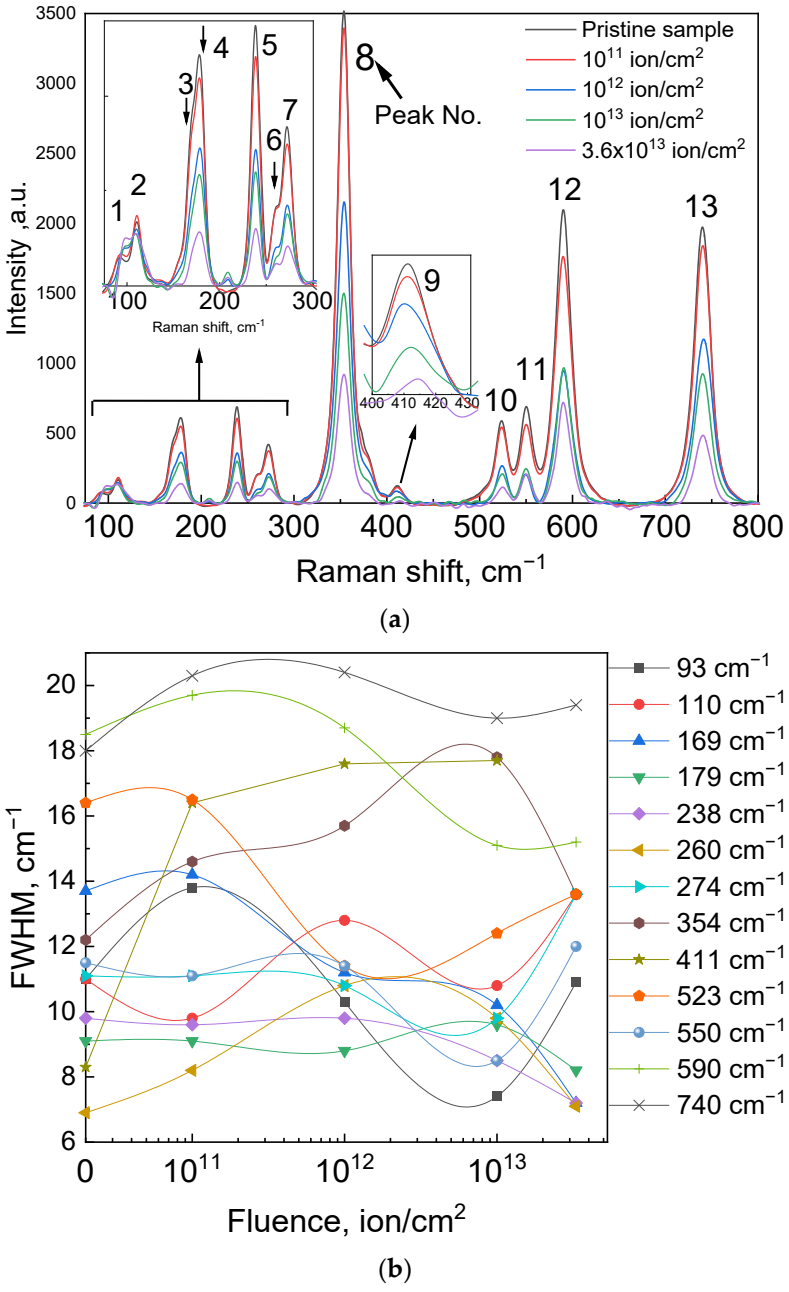

Figure 3. Baseline corrected Raman spectra of GGG single crystals: Pristine and ^{131}Xe ion-irradiated with E = 231 MeV by various fluences (**a**); increase in the Raman line width (FWHM) with increasing ^{131}Xe fluence (**b**).

Table 1 summarizes the measured positions of the main Raman peaks (band maxima) for pristine and irradiated GGG crystals, along with the corresponding full widths at half maximum (FWHM) for the same modes (Figure 3b). Data are provided for all prominent first-order modes with E_g, T_{2g}, and A_{1g} symmetries within the sensitivity range of the spectrometer. Raman peak positions and full widths at half maximum (FWHM) were determined after baseline correction by fitting individual bands with Voigt profiles. The peak position uncertainty was estimated to be ± 1 cm^{-1}, while the uncertainty in FWHM was ± 1–2 cm^{-1}, based on repeated measurements at different surface positions and fitting reproducibility. These uncertainties are comparable to the marker size used in the figures and therefore are not explicitly shown as error bars. For instance, the E_g mode at ~260 cm^{-1} shifts by less than 1 cm^{-1} (from ~259.7 cm^{-1} in the pristine sample to ~259.5 cm^{-1} at 3.3×10^{13} ions/cm^2), while the T_2g line at 274 cm^{-1} slightly increases in frequency (from

~272.6 cm^{-1} to ~274.0 cm^{-1}, within the experimental uncertainty). The high-frequency mode at ~740 cm^{-1} (T_{2g}) remains practically unchanged (<1 cm^{-1}). These observations indicate that no large-scale weakening of lattice bonds occurs—even with defect accumulation, the frequencies of internal vibrations remain close to their initial values.

Table 1. Positions of Raman peak maxima and full widths at half maximum (FWHM, cm^{-1}) of the main vibrational modes of GGG before and after irradiation with ^{131}Xe ions (231 MeV) at various fluences.

Mode (sym.)	Pristine	Pristine	F = 10^{11} ion/cm^2		F = 10^{12} ion/cm^2		F = 10^{13} ion/cm^2		F = 3.3 × 10^{13} ion/cm^2	
	Position (cm^{-1})	FWHM (cm^{-1})	Position (cm^{-1})	FWHM (cm^{-1})	Position (cm^{-1})	FWHM (cm^{-1})	Position (cm^{-1})	FWHM (cm^{-1})	Position (cm^{-1})	FWHM (cm^{-1})
~93 (T_{2g})	92.9	11.0	92.9	13.8	96.0	10.3	97.5	7.4	99.1	10.9
110 (E_g)	110.0	11.0	110.0	9.8	110.2	12.8	109.3	10.8	111.1	13.6
169 (T_{2g})	169.7	13.7	170.1	14.2	170.4	11.2	170.4	10.2	172	7.2
179 (T_{2g})	179.0	9.1	179.1	9.1	179.2	8.8	178.8	9.6	179.4	8.2
238 (T_{2g})	238.3	9.8	238.3	9.6	238.5	9.8	238.1	8.5	238.6	7.2
260 (E_g)	259.7	6.9	260.2	8.2	260.5	10.8	260.5	9.8	259.5	7.1
274 (T_{2g})	272.6	11.1	272.8	11.1	273.1	10.8	272.4	9.8	274.0	13.6
354 (A_{1g})	354.0	12.2	353.7	14.6	353.7	15.7	353.6	17.8	353.1	13.6
411 (T_{2g})	411.2	8.3	411.0	16.4	410.4	17.6	410.4	17.7	415	-
523 (A_{1g})	523.0	16.4	523.3	16.5	523.9	11.4	524.6	12.4	524.9	13.6
550 (T_{2g})	550.1	11.5	550.0	11.1	549.0	11.4	550.0	8.5	549.2	12.0
~590 (T_{2g})	590.2	18.5	590.1	19.7	590.6	18.7	590.6	15.1	590.3	15.2
740 (T_{2g})	740.4	18.0	740.2	20.3	741.1	20.4	739.9	19.0	740.4	19.4

As seen from Table 1, most mode frequencies remain nearly unchanged up to the maximum irradiation dose, indicating the preservation of local force constants for vibrations within structural units (particularly for the strong Ga-O bonds). Notably, the high-frequency T_{2g} mode (~740 cm^{-1}), corresponding to valence vibrations of the stiffest Ga-O bonds, exhibited the least sensitivity to irradiation—its frequency remains within the experimental uncertainty, and its linewidth increased only slightly (discussed in detail below). In contrast, low-energy modes (<200 cm^{-1}), mainly associated with translations of the heavy Gd^{3+} sublattice and collective bending vibrations of the framework, are considerably "softer": their frequencies decrease under irradiation, and the modes degrade and damp more rapidly. For example, the T_{2g} mode at ~169 cm^{-1}, as previously noted, disappears at the maximum fluence. Thus, the most radiation-resistant modes are the high-frequency internal vibrations of structural polyhedra (particularly GaO_4 tetrahedra), whereas the least resistant are low-frequency modes related to vibrations of the entire crystal framework and heavy nodes (Gd). This conclusion aligns with general knowledge on garnet lattice dynamics and previous experiments: neutron irradiation of GGG resulted in the disappearance of fine high-frequency second-order structures (1350–1550 cm^{-1}) and the appearance of diffuse bands in the 100–850 cm^{-1} range, indicating dominance of defect-induced vibrations and long-range mode disorder [30–34].

The primary effect of irradiation on GGG Raman spectra is pronounced broadening of all first-order scattering lines. As shown in Figure 3b, at fluences of 10^{12}–10^{13} ions/cm^2, initially narrow peaks become significantly broader and lower in intensity, and at the maximum dose, some peaks almost merge. The presented Figure 3b illustrates two distinct behaviors of Raman line broadening in GGG single crystals irradiated with 231 MeV ^{131}Xe ions. In the first case, the linewidths increase monotonically Figure 3b with rising ion fluence, reflecting a progressive growth of radiation-induced disorder. The most pronounced broadening is observed for the high-frequency A_{1g} (354 cm^{-1}) and T_{2g} (411 cm^{-1}) modes,

which correspond to internal vibrations of GaO_4 polyhedra. The highest-frequency T_{2g} mode at ~740 cm^{-1} shows only a weak linewidth variation that remains comparable to the experimental uncertainty. Because these bonds are the strongest within the garnet lattice, their broadening is primarily caused by enhanced inelastic phonon-defect scattering rather than bond rupture. The systematic FWHM increase in these modes thus indicates the accumulation of microdefects while preserving the overall crystalline order, representing radiation-induced lattice disorder without complete amorphization. Accordingly, conclusions about irradiation-induced disorder are drawn from consistent linewidth trends across multiple Raman modes, rather than from marginal changes in individual peaks.

In contrast, other modes display non-monotonic variations in linewidth with fluence (Figure 3b). For low-energy vibrations in the 93–179 cm^{-1} range, associated with Gd^{3+} translations and framework deformations, an initial broadening is followed by partial narrowing or even disappearance of the peaks at fluences above 10^{13} ions/cm^2. This behavior arises from a competition between amorphization and local recrystallization: at low doses, lattice distortions dominate, increasing FWHM, while at high doses, overlapping ion tracks and vibrational averaging within a defect-rich matrix may lead to an apparent narrowing of the bands. Several intermediate-frequency modes (238, 260, 274, 550, 590 cm^{-1}) exhibit complex trends due to overlapping neighboring lines and decreasing spectral resolution, further emphasizing the intricate interplay between defect formation, phonon scattering, and partial structural recovery in irradiated GGG. The ~549–550 cm^{-1} mode lies between two much stronger bands centered at ~523 and ~590 cm^{-1}. With increasing fluence, the substantial broadening of these neighboring modes leads to enhanced spectral overlap in the 540–560 cm^{-1} range, which introduces additional uncertainty in the fitting of the ~550 cm^{-1} component. Consequently, the apparent intensity or linewidth increase observed at 10^{12} ion/cm^2 is considered afitting-related effect rather than a distinct irradiation-induced structural change.

Table 1 demonstrates the increase in FWHM for several key modes. On average, linewidths increase by 20–50% from the pristine crystal to fluences of ~10^{13} ions/cm^2. For certain modes, broadening is more pronounced: for example, the T_2g mode at ~411 cm^{-1} initially had FWHM ~8.3 cm^{-1}, but broadened to ~17–18 cm^{-1} at 10^{12}–10^{13} ions/cm^2 and almost vanished at 3.3×10^{13} ions/cm^2. Similarly, the low-frequency mode at ~169 cm^{-1} (initially ~13.7 cm^{-1}) becomes undetectable at the highest fluence. These observations reflect reduced phonon lifetimes due to inelastic scattering on numerous radiation defects and local lattice distortions. As defect concentration increases, the probability of phonon scattering rises, leading to rapid damping of coherent vibrations (increased gamma width). At high fluences, phonons lose quasi-particle definition, and the spectrum approaches that of an amorphous material [24,32].

Several characteristic trends are apparent from Table 1. First, the linewidth broadening is not strictly monotonic with fluence for each mode. For example, the FWHM of the 238 cm^{-1} (T_2g) mode stays around 9.6–9.8 cm^{-1} up to 10^{12} ion/cm^2 and then decreases to 8.5 and 7.2 cm^{-1} at 10^{13} and 3.3×10^{13} ion/cm^2, respectively. This behavior indicates that, at high damage levels, the low-frequency lattice vibrations are affected not only by cumulative disorder but also by strain redistribution and spectral-weight transfer within the low-wavenumber region, so that the residual band appears narrower although the underlying phonon coherence is reduced. A related effect is seen for the pair of modes near 260 cm^{-1} (E_g) and 274 cm^{-1} (T_{2g}), whose individual lines progressively merge into a single broadened band around 265–270 cm^{-1} at the highest fluences, complicating a separate analysis of each mode. Such non-monotonic linewidth evolution of low-frequency modes in heavily disordered garnets is consistent with earlier observations reported in [31].

Second, the absolute linewidth increase (FWHM in cm^{-1}) is more pronounced for low- and mid-frequency lines. For example, the FWHM of the E_g mode (~110 cm^{-1}) increased by ~6 cm^{-1} (from ~11 to ~17 cm^{-1}, ~+55%), whereas the A_{1g} mode at 354 cm^{-1} increased only by ~1–2 cm^{-1} (~+10%). The high-frequency T_{2g} mode at ~740 cm^{-1} broadened by only ~1–2 cm^{-1} (~+10%). Thus, relative broadening is largest for narrow modes with small initial linewidths (i.e., low-energy and well-resolved modes). Overall, FWHM increases of 10–20% at 10^{13} ions/cm^2 and ~50–100% at 3.3×10^{13} ions/cm^2 correlate with increased lattice disorder and a higher fraction of amorphized material. Similar effects were reported for neutron-irradiated GGG, with notable linewidth broadening at $\phi \approx 10^{18}$ n/cm^2 [24]. At even higher damage levels, complete disappearance of individual vibrational modes and transformation into a two-peak continuum can be expected, as observed in $Y_3Fe_5O_{12}$ at fluences $\geq 10^{14}$ ions/cm^2 [32].

3.2.3. Model of Radiation-Induced Structural Degradation

Different Raman modes exhibit different sensitivity to irradiation-induced disorder, reflecting the heterogeneous response of the vibrational subsystems within the lattice. To compare the "dose → structural response" metric for each mode across series and to remove the influence of laser power, focus, thickness, collection coefficient, and other instrumental factors, a special Raman spectral processing technique was developed. It should be emphasized that the absolute Raman intensity cannot be uniquely attributed to the crystalline matrix fraction because both the amorphous track cores and the defect-rich crystalline regions contribute to the attenuation of phonon coherence and scattering efficiency. For this reason, absolute intensity values were not interpreted as a direct measure of the remaining undamaged volume, in contrast to the case of purely Poisson-type disorder accumulation.

For each spectrum $S(\nu,\Phi)$, the following were performed: (i) baseline correction (linear background in band-free regions), (ii) frequency referencing using a fixed high-frequency reference, and (iii) band approximation by a sum of narrow functions (Lorentz-Voight) with equal instrumental contributions. From these approximations, the positions $\nu_{pk}(\Phi)$, half-widths $\Gamma_{pk}(\Phi)$, and integrated intensities I_{pk} were obtained. To exclude instrumental and geometric factors (power/focus/thickness), we introduce internal normalization based on the strong support band of the lattice at about 355 cm^{-1} (breathing of the GaO_4/GaO_6 framework):

$$R_{pk}(\Phi) = \frac{I_{main}(\Phi)}{I_{pk}(\Phi)} \quad (1)$$

where $I_{main}(\Phi)$ is the integral intensity of the reference band (~355 cm^{-1}). The first metric $R_{pk}(\Phi)$ is shown in Figure 4a,b (for low- and high-frequency modes separately). To compare the dose series, a normalized stability metric was introduced for each mode $\eta_{pk}(\Phi)$ is in Figure 4c (curve "Per-peak normalized response vs. fluence (includes pristine)"). To assess the local kinetics of defect accumulation, the piecewise logarithmic slope between adjacent doses was calculated:

$$\eta_{pk}(\Phi) = \frac{R_{pk}(\Phi)}{R_{pk}(0)} \quad (2)$$

The kinetics of damage accumulation between adjacent doses was estimated using a piecewise logarithmic slope:

$$\left.\frac{d\ln \eta_{pk}}{d\ln \Phi}\right|_{\Phi_{mid}} \approx \frac{\ln \eta_{pk}(\Phi_2) - \ln \eta_{pk}(\Phi_1)}{\ln \Phi_2 - \ln \Phi_1}, \Phi_{mid} = \sqrt{\Phi_1 \Phi_2} \quad (3)$$

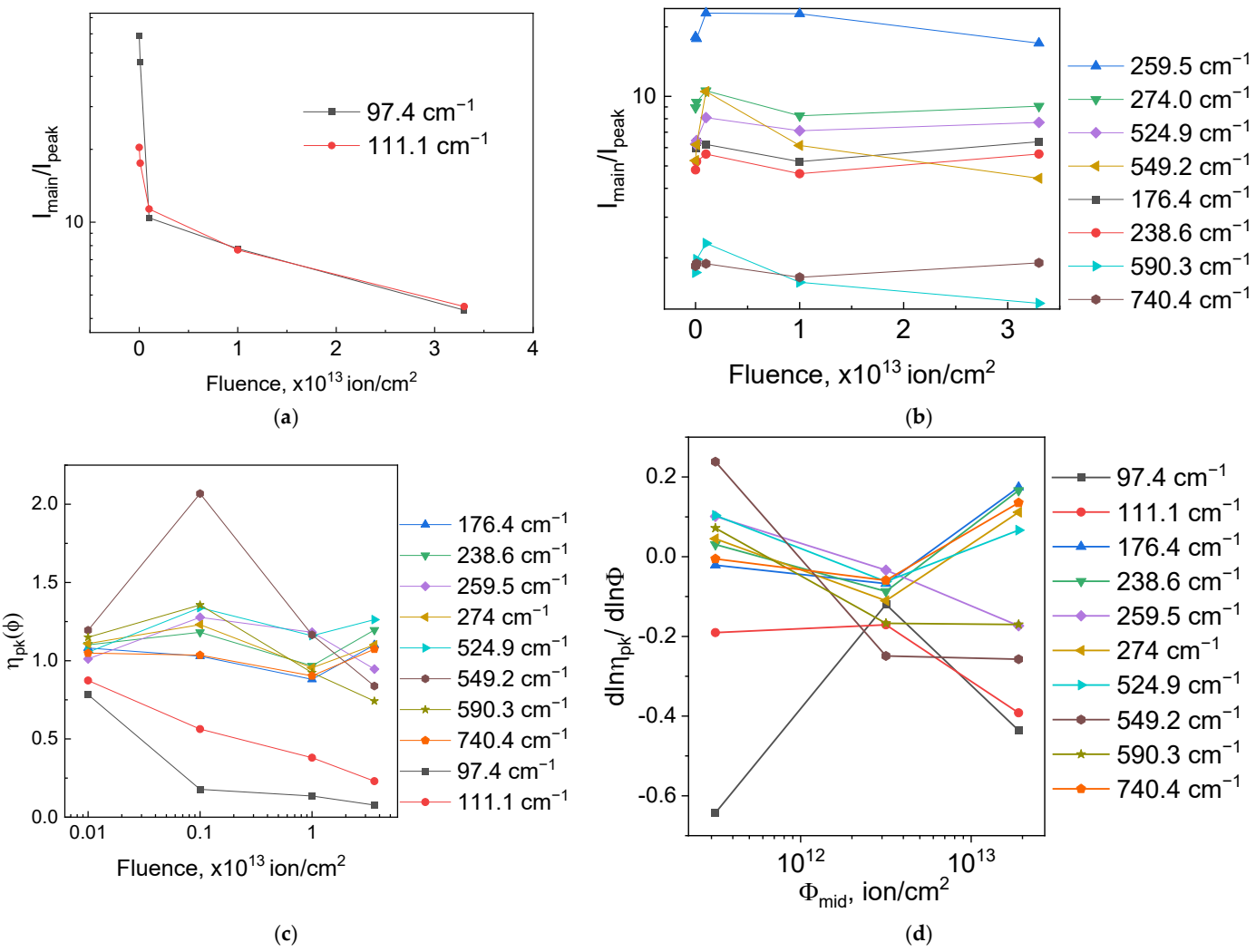

Figure 4. I_{main}/I_{peak} (**a**,**b**); Per-peak normalized response vs. fluence (includes pristine), Degradation rate vs. fluence (**c**), Local degradation kinetics of Raman modes derived from logarithmic slopes (**d**).

The line width as a marker of defective scattering was analyzed according to the dependence:

$$\Gamma_{pk}(\Phi) = \Gamma_{pk}(0) + A_{pk}\,\Phi^{p_{pk}} \tag{4}$$

Swift ^{131}Xe ions generate amorphous cylinders (latent tracks) of radius R∼5 −10 nm via the inelastic thermal spike. The disordered volume fraction is $f(\Phi) = 1 - \exp\left(-\pi R^2 \Phi\right)$ Assuming the crystalline contribution to a mode scale as $(1 - f)^{(\alpha_p k)}$:

$$\eta_{pk}(\Phi) \approx \left[\frac{1 - f(\Phi)}{1 - f(0)}\right]^{\Delta\alpha_{pk}} \tag{5}$$

and the corresponding log-log rate

$$\frac{d\ln \eta_{pk}}{d\ln \Phi} \approx -\Delta\alpha_{pk}\,\frac{\pi R^2 \Phi\, e^{-\pi R^2 \Phi}}{1 - e^{-\pi R^2 \Phi}} \tag{6}$$

Equations (5) and (6) reproduce the three regimes visible in Figure 4c,d: (i) small slopes at low Φ (isolated tracks), (ii) a sharp increase in $d\ln\eta/d\ln\Phi$ near track overlap, (iii) saturation at the highest dose.

The normalized curves $\eta_{pk}(\Phi)$ in Figure 4c exhibit a near-universal "S-shaped" response—incubation at low doses. At high fluences, the observed changes do not originate from further amorphization of already amorphous track regions, but rather from the progressive accumulation of strain and point defects in the remaining crystalline matrix. Quantitatively, the softest low-frequency mode at 97.4 cm^{-1} loses coherent amplitude almost immediately: already at 10^{11} ions/cm^2, $\eta_{97.4}$ falls to $\lesssim$0.05 and remains near zero with further dose increase. The next most sensitive mode, 111.1 cm^{-1}, shows a stepwise decay $\eta_{111.1}$ approx 0.6 $\rightarrow$ 0.45 $\rightarrow$ 0.25 across $10^{11} \rightarrow 10^{12} \rightarrow 10^{13}$ ions/cm^2, corresponding to an aggregate loss of $\sim$60–75% relative to pristine. For mid-frequency modes at 176.4, 238.6, 259.5, and 274.0 cm^{-1} the degradation is moderate: within 10^{12}–10^{13} ions/cm^2, η_{pk} remains in the $\sim$0.7–1.0 corridor, with a small "shelf" or slight recovery for 238.6/274.0 cm^{-1}, indicating competition between track accumulation and local distortion and deformation of GaO_4/GaO_6 polyhedra inferred from Raman linewidth broadening. It should be emphasized that Raman spectroscopy does not provide direct evidence for long-range structural rearrangement; the present interpretation is limited to local distortions and loss of vibrational coherence. Such pronounced local distortions become apparent mainly at high fluences due to the cumulative overlap of strain fields and point-defect populations in the crystalline matrix surrounding amorphous ion tracks. The stiff high-frequency Ga-O stretching modes (549.2, 590.3, 740.4 cm^{-1}) are the most resilient: at 10^{11}–10^{12} ions/cm^2, $\eta_{pk} \approx$ 1.0–1.2 , and by 10^{13} ions/cm^2 they decline only to $\sim$0.8–1.0; the 740.4 cm^{-1} mode remains close to unity across the entire dose range, quantitatively establishing its radiation hardness relative to the reference band.

The kinetics of this behavior is quantified in Figure 4d via the piecewise logarithmic slope. In the low-dose regime, slopes for all modes are near zero, consistent with isolated tracks and dominant elastic relaxation. Within the overlap window 10^{12}–10^{13} ions/cm^2, low- and mid-frequency lines attain their most negative values: for 97.4 cm^{-1} the slope reaches approximately—0.6–0.8), for 111.1 cm^{-1}—0.3–0.5), and for 238.6/259.5 cm^{-1} about $-$0.2–0.3. This is the signature of amorphous-fraction percolation: the rate of coherent-amplitude loss is maximal precisely where track overlap dominates and the probability of traversing regions with disrupted long-range order rises sharply. At the highest dose of 3.3×10^{13} ions/cm^2, the absolute slope decreases; for the high-frequency modes 549.2–740.4 cm^{-1} the slopes become near-zero or even slightly positive ($\lesssim$+0.1).

The quantitative intensity trends are consistent with the evolution of FWHM. According to the provided table, the 97.4 cm^{-1} band exhibits a strong profile restructuring: $\Gamma_{97.4}$ decreases from 58.9 to 4.33 cm^{-1} as the fluence increases from 0 to 3.3×10^{13} ions/cm^2; such "narrowing" against an almost vanishing $\eta_{97.4}$ is a spectral artifact of strong disorder, caused by band coalescence and the wash-out of tails into the background. For 111.1 cm^{-1}, the FWHM grows from 20.4 to $\sim$22 cm^{-1} at intermediate doses and then decreases to 4.48 cm^{-1} at the highest dose, again indicating relabeling of components when background scattering dominates. In the mid-frequency region, a characteristic non-monotonicity appears: for 259.5 cm^{-1}, Γ increases from 18.08 to 22.94 cm^{-1} by 10^{12} ions/cm^2 and then decreases to 16.99 cm^{-1} at 3.3×10^{13} ions/cm^2, coinciding with the fluence at which $|d\ln\eta/d\ln\Phi|$ is maximal and pinpointing the peak of inhomogeneous strain specifically in the overlap window. For 524.9 cm^{-1}, the width grows modestly from 6.22 to 8.09 cm^{-1} by 10^{12} ions/cm^2 and then stabilizes in the 7.1–7.7 cm^{-1} corridor; 549.2 cm^{-1} shows a stronger non-monotonicity (from 5.27 to 10.50 cm^{-1} at 10^{12} ions/cm^2 with a subsequent decrease to 4.42 cm^{-1}), whereas 590.3 and 740.4 cm^{-1} remain narrow throughout (1.27–2.31 and 1.65–1.90 cm^{-1}, respectively), confirming their structural robustness. These quantitative facts align with the overall picture: the largest $|d\ln\eta/d\ln\Phi|$ values in panel (d) occur

precisely where FWHM records the greatest inhomogeneous strain; as the system enters saturation, both η_{pk} and Γ_{pk} stabilize.

3.3. Microhardness and Radiation-Induced Softening

Radiation-induced defects influence not only the vibrational spectra but also the macroscopic properties of GGG, particularly its mechanical hardness. Nanoindentation, as a structure-sensitive method, was employed to investigate the depth distribution of the amorphized zone in GGG single crystals irradiated with 231 MeV ^{131}Xe ions at various fluences. The microhardness (nanohardness) measurements of irradiated crystals reveal pronounced softening under ^{131}Xe ion irradiation. The relative softening effect was quantified as $(H_0 - H)/H_0$, where H_0—is the hardness of the pristine crystal. The mechanical hardness reflects the combined response of amorphous regions (a) and the defect-strained crystalline matrix (b): the pristine hardness corresponds predominantly to region (b), whereas the hardness at the highest fluence approaches the response of a largely amorphized material. Since Raman intensities are likewise governed by the joint contribution of regions (a) and (b), the observed correlation between Raman degradation metrics and hardness evolution is physically meaningful and does not rely on a one-to-one correspondence with a single structural component.

Measurements along cleaved cross-sections in the ion beam direction indicate that samples irradiated at 10^{11} ^{131}Xe ions/cm^2 exhibit hardness values comparable to pristine GGG. Significant hardness reduction occurs at fluences of 10^{12}, 10^{13}, and 3.3×10^{13} ions/cm^2 (Figures 5 and 6). Pristine GGG has a hardness of ~11 GPa. At saturation, softening for 10^{12} ions/cm^2 irradiation exceeds 20%, while for 10^{13} and 3.3×10^{13} ions/cm^2 fluences, it reaches up to 59% (Figure 5), suggesting an upper limit of softening corresponding to full amorphization of GGG

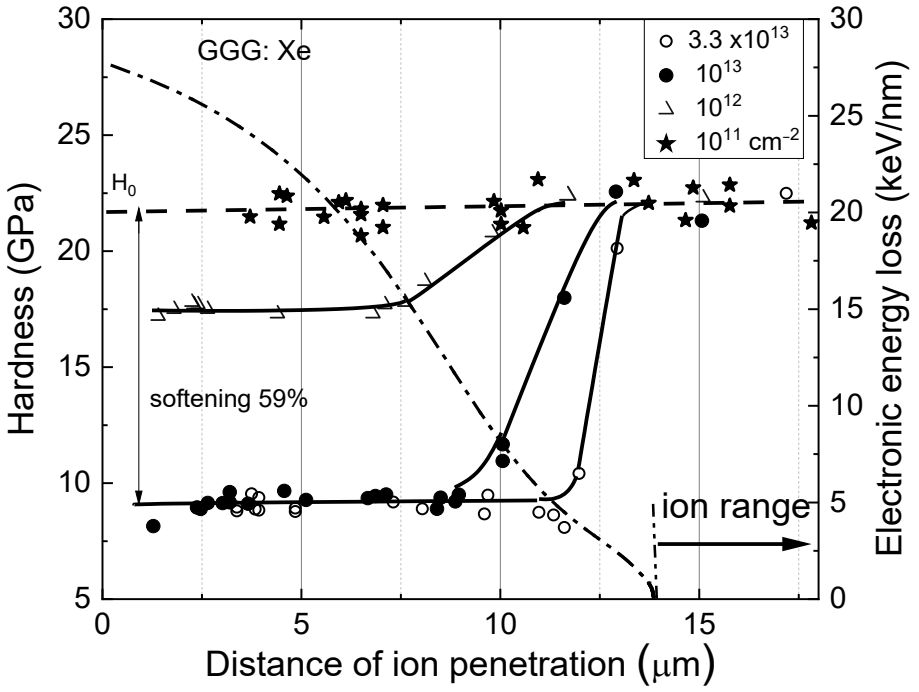

Figure 5. Depth profiles of nanohardness for GGG single crystals irradiated with 231 MeV ^{131}Xe ions at various fluences, and the corresponding electron energy loss density calculated using SRIM. H_0-indicates the hardness of pristine GGG.

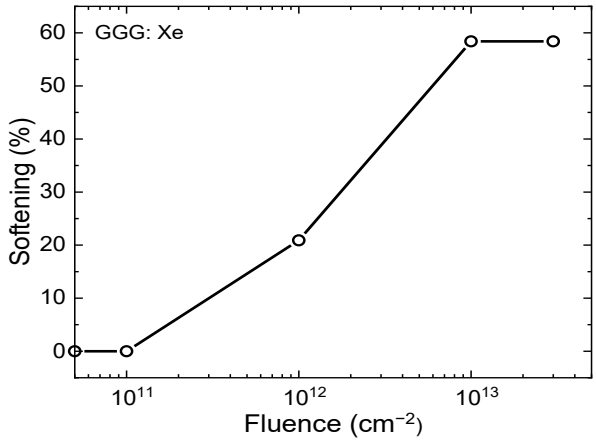

Figure 6. Ion-induced softening of GGG single crystals as a function of electronic energy flux density. Data were derived from Figure 5 using the hardness values at the saturation stage.

The hardness profile along the surface provides insight into the depth distribution of the amorphized layer. The zone of maximum softening extends to ~8.9 μm for F = 10^{13} ions/cm^2 and ~11.3 μm for F = 3.3 × 10^{13} ions/cm^2. The corresponding threshold energy loss for maximum softening is 10.9 and 5.2 keV/nm, respectively (Figure 5).

It should be noted that the calculated electronic stopping thresholds (dE/dx) for GGG are ~6–7 keV/nm. ^{131}Xe ions at 231 MeV possess specific energy losses of 20–30 keV/nm near the surface, far exceeding the track formation threshold. Consequently, each ion creates a cylindrical amorphous track along its trajectory. At fluences of ~10^{13} ions/cm^2, these tracks begin to overlap, forming a continuous damaged network, which accounts for the sharp decrease in hardness. Depth profiles show that the maximum softening occurs near the surface and extends to ~8–12 μm (for fluences 10^{13}–3.3 × 10^{13} ions/cm^2), corresponding to the ^{131}Xe ion range in GGG (~10–15 μm, estimated via SRIM). It should be noted that this pattern of track development and evolution is typical for many dielectrics [49–61]. Moreover, the application of Raman spectroscopy and the investigation of defect-induced Raman modes have, to date, been addressed to a much lesser extent [62–71].

The observed hardness reduction is consistent with previous studies. For instance, irradiation of GGG with 150 MeV Kr ions at fluences of 10^{13}–10^{14} ions/cm^2 also resulted in significant microhardness decrease (~65% of the pristine value) [27], attributed to ion-induced amorphization and associated reduction in material density and elastic modulus. In the present ^{131}Xe experiments, the softening is even more pronounced (hardness drops to ~40%), as expected due to the higher ^{131}Xe ion energy and greater track density. Thus, the radiation resistance of GGG in terms of mechanical integrity is limited to fluences of ~10^{12} ions/cm^2; higher doses induce structural degradation up to partial amorphization, accompanied by substantial softening. The observed microstructure on the fracture surfaces of irradiated samples is characteristic of plastic deformation in amorphous or fine-grained materials and indicates the presence of an amorphous phase. Nanoindentation measurements reveal ion-induced softening, which becomes significant at fluences above 10^{11} ions/cm^2 and reaches ~59% at fluences of 10^{13} and 3.3 × 10^{13} ions/cm^2, approaching saturation. At this stage, near-complete amorphization of the irradiated layer is assumed. The hardness depth profiles provide information on the distribution of the amorphized zone, and threshold values of energy loss for maximum softening and full amorphization have been determined.

For cross-sectional analysis, the irradiated samples were mechanically cleaved along natural fracture planes without polishing or ion milling. The irradiation surface was not mechanically treated and was spatially separated from the fracture edge; therefore, the

cleaving procedure is not expected to affect the irradiation-modified near-surface region. Figure 7 illustrate large-scale surface morphology and fracture features after irradiation. Individual ion tracks are not expected to be resolved at this spatial scale. The arrow indicates the ion beam direction.

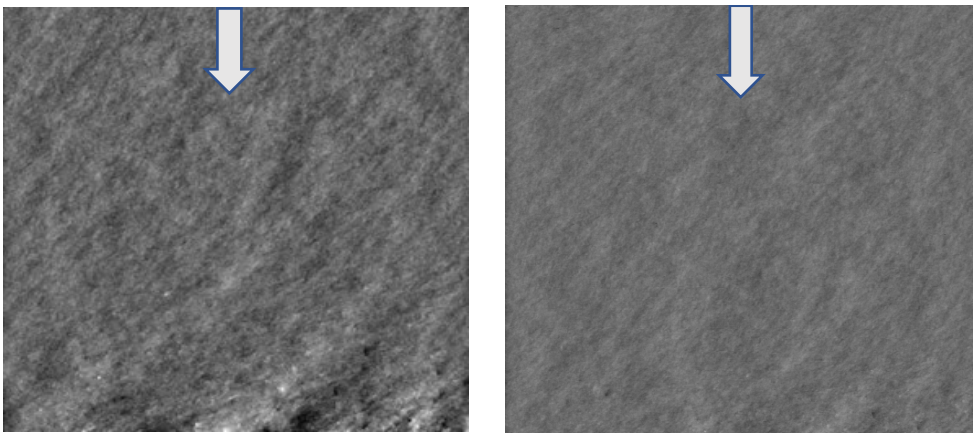

(**a**) (**b**)

Figure 7. AFM images of the cleaved surface of GGG irradiated with 231 MeV ^{131}Xe ions (fluence 10^{13} ions/cm^2). Image areas are 5 × 5 μm^2 (**a**) and 8 × 8 μm^2 (**b**). The arrow indicates the ion beam direction.

The fluence dependence of micro/nanohardness (H/H_0) mirrors the Raman metrics from Figure 4c,d: the normalized per-mode response $\eta_{pk}(\Phi)$ and its log-log slope act as structurally sensitive damage markers that rise and fall in lockstep with mechanical degradation. In the low-dose regime ($\leq 10^{11}$–10^{12} ions/cm^2), η_{pk} remains near unity and the slopes are ~0, consistent with isolated tracks and rapid elastic relaxation; (H/H_0) is essentially unchanged. Entering the overlap window (10^{12}–10^{13} ions/cm^2), η_{pk} collapses different modes exhibit different sensitivity to radiation-induced disorder and the slopes reach their most negative values precisely where (H/H_0) develops its steepest decline—both signatures of percolating amorphous tracks and a rapid rise in the disordered volume fraction. At the highest fluence (3.3×10^{13} ions/cm^2), the slopes relax toward zero and (H/H_0) approaches a plateau, indicating damage saturation and possible dynamic annealing.

Quantitatively, the softest lattice modes are the best early predictors of hardness loss: the 97.4 cm^{-1} line loses coherent amplitude almost immediately ($\eta_{97.4} \lesssim 0.05$) by 10^{11} ions/cm^2), while 111.1 cm^{-1} steps from $\approx$0.6 $\rightarrow$ 0.45 $\rightarrow$ 0.25 across $10^{11} \rightarrow 10^{12} \rightarrow 10^{13}$ ions/cm^2. Mid-frequency modes (176.4, 238.6, 259.5, 274.0 cm^{-1}) degrade more moderately (typical overlap-window slopes ≈ -0.2 to -0.3), matching the inflection of ($H/H_0(\Phi)$). In contrast, rigid Ga-O stretches (549.2, 590.3, 740.4 cm^{-1}) retain ($\eta_{pk} \approx 0.8 - 1.0$) up to ~$10^{13}$ ions/cm^2 and show near-zero or slightly positive slopes at the end of the dose series; (H/H_0) is simultaneously on its saturation plateau. FWHM trends corroborate this coupling: linewidths peak (or show strongest non-monotonicity) in the same overlap window where the Raman slopes are most negative and the hardness drop is fastest, evidencing maximal inhomogeneous strain and phonon-defect scattering.

The correlation with hardness is established at the level of damage stages and mode families, not by selectively matching individual peaks, and the low-frequency modes were chosen as examples precisely because they probe the same mechanically fragile sublattice that controls the macroscopic hardness.

Practically, these results justify using $\eta_{pk}(\Phi)$ and its slope as non-destructive predictors of mechanical degradation. Low-frequency modes flag the onset of damage that triggers

the hardness drop, whereas high-frequency Ga-O stretches track the residual structural integrity that governs the hardness plateau at high fluence.

At low fluences ($\leq 10^{11}$–10^{12} ion/cm^2), irradiation-induced damage in GGG is governed by isolated point defects and small defect aggregates formed in the crystalline matrix surrounding spatially separated amorphous ion tracks. In this regime, Raman spectra exhibit moderate linewidth broadening and intensity reduction in low-frequency lattice modes, while high-frequency Ga–O stretching modes remain relatively stable. The microhardness shows only minor changes, indicating that elastic strain fields and point defects do not yet strongly affect the load-bearing framework.

At intermediate fluences ($\approx 10^{11}$–10^{12} ion/cm^2), defect accumulation becomes nonlinear due to overlap of strain fields and partial overlap of ion tracks. Enhanced defect clustering and increasing lattice distortion reduce phonon coherence, leading to pronounced Raman peak broadening, spectral overlap, and increased background scattering. Concurrently, the hardness decreases significantly, reflecting the growing contribution of disordered and locally amorphized regions.

At the highest fluences ($\geq 10^{13}$ ion/cm^2), overlapping ion tracks form an extended disordered network in the near-surface layer. In this regime, extended defects and locally amorphized volumes dominate both vibrational and mechanical responses. Low-frequency Raman modes are strongly suppressed, whereas high-frequency Ga–O modes persist due to the rigidity of internal polyhedral bonds. The hardness approaches saturation, consistent with extensive amorphization. Overall, radiation-induced disorder in GGG evolves through successive stages of point-defect formation, defect clustering, and track overlap, which are consistently reflected in both Raman and hardness measurements.

The present results show that 231 MeV ^{131}Xe ions induce a heterogeneous damage pattern in GGG that cannot be described by a single "universal" damage curve. Raman spectroscopy demonstrates that all fundamental garnet modes remain observable up to 3.3×10^{13} ions/cm^2, while their linewidths increase and their contrast decreases. Nanoindentation, in turn, reveals a $\approx$60% hardness reduction in the same fluence range. This behavior is consistent with a two-phase picture in which amorphous ion-track cores are embedded in a defect-rich crystalline matrix; Raman and hardness both probe this composite system, but with different weightings of its components, so an exact one-to-one correspondence of their fluence dependences is not expected.

Raman data indicate that GGG does not undergo a wholesale phase transformation under the present irradiation conditions: all first-order garnet modes remain detectable and no new sharp lines of secondary crystalline phases appear. At the same time, the growth of a broad background and the merging of individual bands at high fluence clearly signal the formation of locally amorphous or strongly distorted regions along the ion tracks. In this sense, "structural stability" refers to the preservation of the garnet topology and the absence of macroscopic recrystallization into another phase, rather than to the absence of local amorphization inside tracks.

The evolution of Raman parameters with fluence is naturally mode-dependent and not strictly monotonic. Under swift heavy-ion irradiation the system passes from isolated tracks to a track-overlap regime and finally to partial saturation with stress relaxation [31–34]. Linewidths and intensities therefore reflect a competition between defect accumulation, relaxation and vibrational averaging over an increasingly heterogeneous volume. Low-frequency modes below ~200 cm^{-1}, associated with Gd-sublattice translations and framework deformations, as well as mid-frequency modes near 238–260 and 354–411 cm^{-1}, exhibit the strongest broadening and loss of contrast, consistent with their sensitivity to network disorder. In contrast, high-frequency Ga-O stretching modes near 740 cm^{-1} remain comparatively narrow and nearly invariant in frequency, reflecting the

robustness of the stiffest Ga-O bonds and serving as an internal marker of preserved local polyhedral structure.

Within this framework, the relationship between Raman metrics and hardness must be understood as qualitative and phenomenological but physically motivated description based on the well-established track-formation and track-overlap scenario in garnets. Hardness is an integral measure of the load-bearing capacity of the damaged layer, governed by the percolation and connectivity of stiff regions and amorphous tracks, whereas Raman spectroscopy primarily reports on the crystalline fraction and the coherence of its phonon modes. The key point is that the fluence interval where hardness decreases most steeply (10^{12}–10^{13} ions/cm^2) coincides with the range where low- and mid-frequency Raman modes show maximal broadening and loss of contrast, and where the background increases strongly. At the highest fluence, hardness approaches a saturation level corresponding to a largely amorphized near-surface layer, and the Raman spectra evolve towards broad bands characteristic of a highly disordered garnet. For comparison with hardness we therefore use the evolution of the low-frequency mode near 97 cm^{-1} and the 238–260 cm^{-1} band as representative of framework-sensitive vibrations, while treating the near-constant Ga-O stretching modes as evidence for the survival of the local GaO_4/GaO_6 units despite the marked loss of macroscopic mechanical rigidity.

Taken together, the combined Raman–nanoindentation analysis places irradiated GGG within the broader family of garnet oxides under high electronic stopping power, where amorphous tracks, a heavily disordered but still garnet-like matrix, and non-trivial (often non-monotonic) evolutions of structural and mechanical observables are a generic consequence of track formation, overlap and partial relaxation. This justifies a phenomenological, rather than purely single-parameter, description of radiation-induced disorder in such complex materials.

4. Conclusions

After irradiation of $Gd_3Ga_5O_{12}$ single crystals with 231 MeV ^{131}Xe ions at fluences ranging from 1×10^{11} to 3.3×10^{13} ions/cm^2, the Raman spectra exhibited distinct quantitative changes reflecting the transition from an ordered to a partially amorphous lattice. At low fluences ($\leq 10^{11}$ ions/cm^2), the spectra remained sharp, with typical linewidths (FWHM) of 8–12 cm^{-1}. At 10^{12}–10^{13} ions/cm^2, FWHM values increased by 20–50%, reaching 16–18 cm^{-1} for the A_{1g} (354 cm^{-1}) and T_{2g} (411 cm^{-1}) modes, indicating enhanced microdefect density and phonon-defect scattering. At the highest fluence of 3.3×10^{13} ions/cm^2, the low-frequency T_2g (169 cm^{-1}) mode disappeared entirely, whereas the high-frequency T_{2g} (~740 cm^{-1}) mode remained stable, with frequency shifts below 1 cm^{-1}, confirming its radiation resilience. These results show that irradiation first disrupts the heavy Gd^{3+} sublattice and collective framework modes, while the internal Ga-O bonds remain structurally intact.

To quantitatively interpret these effects, a new Raman analysis methodology was developed based on internal normalization and logarithmic degradation analysis. Each spectrum $S(\nu, \Phi)$ was normalized to the intensity of the stable A_{1g} (355 cm^{-1}) reference band, and per-mode normalized amplitudes $\eta_{pk} = I_{pk}/I_{355}$ and their logarithmic slopes $d\ln\eta/d\ln\Phi$ were calculated. This approach eliminates variations from laser power, focusing, and sample thickness, allowing direct comparison of the sensitivity of individual modes. The results show that soft modes (<200 cm^{-1}) lose coherence rapidly (η_{pk} dropping from 1 to 0.05 by 10^{11} ions/cm^2), while Ga-O stretching modes (549–740 cm^{-1}) remain nearly constant ($\eta_{pk} \approx 0.8$–1.0 up to 10^{13} ions/cm^2). The local slopes $d \ln \eta / d \ln \Phi$ reach maximum negative values (-0.6 for 97 cm^{-1}, -0.3 for 238–260 cm^{-1}) in the track-overlap region (10^{12}–10^{13} ions/cm^2), coinciding with a pronounced hardness drop ($H/H_0 \approx 0.4$).

Thus, the developed methodology provides the first quantitative link between micromechanical softening and Raman-mode degradation, defining a critical fluence for track percolation (~1–3 × 10^{13} ions/cm^2) and a hardness reduction limit of about 60%. This framework enables non-destructive prediction of radiation-induced damage in oxide scintillator and optoelectronic materials using the parameters η_{pk} and d ln η/d ln Φ.

Author Contributions: Conceptualization, G.M.A., Z.T.K., A.I.P. and A.T.Z.; Methodology, G.M.A., A.T.Z., I.M., S.U. and A.I.P.; Software, A.T.Z., A.B. and Y.S.; Validation, G.M.A., A.T.Z., I.M., G.E.S.,I.M., Y.S. and A.I.P.; Formal analysis, Z.T.K., A.T.Z., A.M.Z., G.E.S., A.S. and Y.S.; Investigation, G.E.S., M.K. and A.I.P.; Resources, G.M.A., A.M.Z., A.T.Z., I.M., M.K. and A.S.; Data curation, Z.T.K., G.M.A., K.B., A.M.Z., A.B., I.M., G.E.S. and A.S.; Writing—original draft preparation, Z.T.K. and K.B.; Writing—review and editing, Z.T.K., K.B., G.M.A. and A.I.P.; Visualization, A.A., A.B. and A.S.; Supervision, G.M.A. and M.K.; Project administration, M.K. and A.I.P.; Funding acquisition, G.M.A. and M.K. All authors have read and agreed to the published version of the manuscript.

Funding: This research was funded by the Science Committee of the Ministry of Science and Higher Education of the Republic of Kazakhstan (Grant No. AP19680626). In addition, Marina Konuhova and Anatoli I. Popov were supported by Latvian research project lzp-2023/1-0453 "Prediction of long-term stability of functional materials under extreme radiation conditions".

Data Availability Statement: The raw data supporting the conclusions of this article will be made available by the authors upon reasonable request.

Conflicts of Interest: The authors declare no conflicts of interest.

References

1. Mkrtchyan, M.; Butaeva, T.; Eganyan, A.; Ovanesyan, K. Absorption and Emitting Properties of GGG:Ce Single Crystals in the Range of 4f–5d Transitions of Ce^{3+} Ions. *Armen. J. Phys.* **2019**, *12*, 273–282.
2. Syvorotka, I.I.; Sugak, D.Y.; Wierzbicka, A.; Wittlin, A.; Przybylińska, H.; Barzowska, J.; Barcz, A.J.; Berkowski, M.; Domagała, J.Z.; Mahlik, S.; et al. Optical Properties of Pure and Ce^{3+}-Doped Gadolinium Gallium Garnet Crystals and Epitaxial Layers. *J. Lumin.* **2015**, *164*, 31–37. [CrossRef]
3. Mikhailov, M.M.; Neshchimenko, V.V.; Shavlyuk, V.V. The Effects of Binding Type on Luminescence LED Phosphor Based on GGG/Ce^{3+}. *Opt. Mater.* **2014**, *38*, 33–36. [CrossRef]
4. Wang, Y.; You, Z.; Li, J.; Zhu, Z.; Ma, E.; Tu, C. Spectroscopic Investigations of Highly Doped Er^{3+}: GGG and Er^{3+}/Pr^{3+}: GGG Crystals. *J. Phys. D Appl. Phys.* **2009**, *42*, 215406. [CrossRef]
5. Wang, Y.; You, Z.; Li, J.; Zhu, Z.; Tu, C. Optical Properties of Dy^{3+} Ion in GGG Laser Crystal. *J. Phys. D Appl. Phys.* **2010**, *43*, 075402. [CrossRef]
6. Liu, W.; Zhang, Q.; Sun, D.; Luo, J.; Gu, C.; Jiang, H.; Yin, S. Crystal Growth and Spectral Properties of Sm:GGG Crystal. *J. Cryst. Growth* **2011**, *331*, 83–86. [CrossRef]
7. Jia, Z.; Tao, X.; Dong, C.; Cheng, X.; Zhang, W.; Xu, F.; Jiang, M. Study on Crystal Growth of Large Size Nd^{3+}:$Gd_3Ga_5O_{12}$ (Nd^{3+}:GGG) by Czochralski Method. *J. Cryst. Growth* **2006**, *292*, 386–390. [CrossRef]
8. Asadian, M.; Hajiesmaeilbaigi, F.; Mirzaei, N.; Saeedi, H.; Khodaei, Y.; Enayati, S. Composition and Dissociation Processes Analysis in Crystal Growth of Nd:GGG by the Czochralski Method. *J. Cryst. Growth* **2010**, *312*, 1645–1650. [CrossRef]
9. Tsiumra, V.; Krasnikov, A.; Zazubovich, S.; Zhydachevskyy, Y.; Vasylechko, L.; Baran, M.; Wachnicki, Ł.; Lipińska, L.; Nikl, M.; Suchocki, A. Crystal Structure and Luminescence Studies of Microcrystalline GGG:Bi^{3+} and GGG:Bi^{3+},Eu^{3+} as a UV-to-VIS Converting Phosphor for White LEDs. *J. Lumin.* **2019**, *213*, 278–289. [CrossRef]
10. Zhou, W.; Zhang, Q.; Xiao, J.; Luo, J.; Liu, W.; Jiang, H.; Yin, S. Sm^{3+}-Doped (Ca, Mg, Zr) GGG Crystal: A Potential Reddish-Orange Laser Crystal. *J. Alloys Compd.* **2010**, *491*, 618–622. [CrossRef]
11. Gluchowski, P.; Chaika, M. Crystal-Field Strength Variations and Energy Transfer in Cr^{3+}-Doped GGG Transparent Nanoceramics. *J. Phys. Chem. C* **2024**, *128*, 9641–9651. [CrossRef]
12. Zhao, G.; Li, T.; Xu, J. Growth of Epitaxial Substrate $Gd_3Ga_5O_{12}$ (GGG) Single Crystal through Pure GGG Phase Polycrystalline Material. *J. Cryst. Growth* **2002**, *237*, 720–724. [CrossRef]
13. Li, C.; Zhang, F.; Meng, B.; Rao, X.; Zhou, Y. Research of Material Removal and Deformation Mechanism for Single Crystal GGG ($Gd_3Ga_5O_{12}$) Based on Varied-Depth Nanoscratch Testing. *Mater. Des.* **2017**, *125*, 180–188. [CrossRef]
14. Li, C.; Wu, Y.; Li, X.; Ma, L.; Zhang, F.; Huang, H. Deformation Characteristics and Surface Generation Modelling of Crack-Free Grinding of GGG Single Crystals. *J. Mater. Process. Technol.* **2020**, *279*, 116577. [CrossRef]

15. Li, C.; Zhang, F.; Wang, X.; Rao, X. Investigation on Surface/Subsurface Deformation Mechanism and Mechanical Properties of GGG Single Crystal Induced by Nanoindentation. *Appl. Opt.* **2018**, *57*, 3661–3668. [CrossRef]
16. Li, H.; Sun, D.; Zhang, H.; Luo, J.; Quan, C.; Qiao, Y.; Dong, K.; Chen, Y.; Wang, Z.; Cheng, M.; et al. Growth, Rietveld Refinement, Raman Spectrum and Dislocation of Ca/Mg/Zr-Substituted GGG: A Potential Substrate and Laser Host Material. *J. Mater. Sci. Mater. Electron.* **2024**, *35*, 12777. [CrossRef]
17. Syvorotka, I.I.; Sugak, D.; Yakhnevych, U.; Buryy, O.; Włodarczyk, D.; Pieniążek, A.; Zhydachevskyy, Y.; Levintant-Zayonts, N.; Savytskyy, H.; Bonchyk, O.; et al. Investigation of the Interface of $Y_3Fe_5O_{12}/Gd_3Ga_5O_{12}$ Structure Obtained by the Liquid Phase Epitaxy. *Cryst. Res. Technol.* **2022**, *57*, 2100180. [CrossRef]
18. Leontsev, S.; Shah, P.J.; Kum, H.S.; McChesney, J.L.; Rodolakis, F.M.; van Veenendaal, M.; Velez, M.; Rao, R.; Haskel, D.; Kim, J.; et al. Functional Properties of Yttrium Iron Garnet Thin Films on Graphene-Coated $Gd_3Ga_5O_{12}$ for Remote Epitaxial Transfer. *J. Magn. Magn. Mater.* **2022**, *556*, 169440. [CrossRef]
19. Tikhonov, V.V.; Litvinenko, A.N.; Sadovnikov, A.V.; Nikitov, S.A. Brillouin Spectroscopy of Nonlinear Magnetoacoustic Resonances in a Layered YIG/GGG Structure. *Bull. Russ. Acad. Sci. Phys.* **2016**, *80*, 1242–1247. [CrossRef]
20. Papagelis, K.; Arvanitidis, J.; Vinga, E.; Christofilos, D.; Kourouklis, G.M.A.; Kimura, H.; Ves, S. Vibrational Properties of $(Gd_{1-x}Y_x)_3Ga_5O_{12}$ Solid Solutions. *J. Appl. Phys.* **2010**, *107*, 113504. [CrossRef]
21. Monteseguro, V.; Rodríguez-Hernández, P.; Ortiz, H.M.; Venkatramu, V.; Manjón, F.J.; Jayasankar, C.K.; Lavín, V.; Muñoz, A. Structural, Elastic and Vibrational Properties of Nanocrystalline $Lu_3Ga_5O_{12}$ under High Pressure. *Phys. Chem. Chem. Phys.* **2015**, *17*, 9454–9464. [CrossRef]
22. Sugak, D.; Syvorotka, I.I.; Yakhnevych, U.; Buryy, O.; Vakiv, M.; Ubizskii, S.; Włodarczyk, D.; Zhydachevskii, Y.; Pieniążek, A.; Jakiela, R.; et al. Investigation of Co Ions Diffusion in $Gd_3Ga_5O_{12}$ Single Crystals. *Acta Phys. Pol. A* **2018**, *133*, 959–964. [CrossRef]
23. Hamilton, A.S.; Lampronti, G.I.; Rowley, S.E.; Dutton, S.E. Enhancement of the Magnetocaloric Effect Driven by Changes in the Crystal Structure of Al-Doped GGG, $Gd_3Ga_5-xAlxO_{12}$ ($0 \leq x \leq 5$). *J. Phys. Condens. Matter* **2014**, *26*, 116001. [CrossRef]
24. Mironova-Ulmane, N.; Sildos, I.; Vasil'chenko, E.; Chikvaidze, G.; Skvortsova, V.; Kareiva, A.; Muñoz-Santiuste, J.E.; Pareja, R.; Elsts, E.; Popov, A.I. Optical Absorption and Raman Studies of Neutron-Irradiated $Gd_3Ga_5O_{12}$ Single Crystals. *Nucl. Instrum. Methods Phys. Res. B* **2018**, *435*, 306–312. [CrossRef]
25. Potera, P.; Matkovskii, A.; Sugak, D.; Grigorjeva, L.; Millers, D.; Pankratov, V. Transient Color Centers in GGG Crystals. *Radiat. Eff. Defects Solids* **2002**, *157*, 709–713. [CrossRef]
26. Potera, P.; Ubizskii, S.; Sugak, D.; Schwartz, K. Induced Absorption in Gadolinium Gallium Garnet Irradiated by High-Energy ^{235}U Ions. *Acta Phys. Pol. A* **2010**, *117*, 181–183. [CrossRef]
27. Karipbayev, Z.T.; Kumarbekov, K.; Manika, I.; Dauletbekova, A.; Kozlovskiy, A.L.; Sugak, D.; Ubizskii, S.B.; Akilbekov, A.; Suchikova, Y.; Popov, A.I. Optical, Structural, and Mechanical Properties of $Gd_3Ga_5O_{12}$ Single Crystals Irradiated with $84Kr^+$ Ions. *Phys. Status Solidi B* **2022**, *259*, 2100415. [CrossRef]
28. Meftah, A.; Costantini, J.M.; Khalfaoui, N.; Boudjadar, S.; Stoquert, J.P.; Studer, F.; Toulemonde, M. Experimental Determination of Track Cross-Section in $Gd_3Ga_5O_{12}$ and Comparison to the Inelastic Thermal Spike Model Applied to Several Materials. *Nucl. Instrum. Methods Phys. Res. B* **2005**, *237*, 563–574. [CrossRef]
29. Toulemonde, M.; Meftah, A.; Costantini, J.M.; Schwartz, K.; Trautmann, C. Out-of-Plane Swelling of Gadolinium Gallium Garnet Induced by Swift Heavy Ions. *Nucl. Instrum. Methods Phys. Res. B* **1998**, *146*, 426–430. [CrossRef]
30. Meftah, A.; Assmann, W.; Khalfaoui, N.; Stoquert, J.P.; Studer, F.; Toulemonde, M.; Trautmann, C.; Voss, K.-O. Electronic Sputtering of $Gd_3Ga_5O_{12}$ and $Y_3Fe_5O_{12}$ Garnets: Yield, Stoichiometry and Comparison to Track Formation. *Nucl. Instrum. Methods Phys. Res. B* **2011**, *269*, 955–958. [CrossRef]
31. Costantini, J.-M.; Miro, S.; Beuneu, F.; Toulemonde, M. Swift Heavy Ion-Beam Induced Amorphization and Recrystallization of Yttrium Iron Garnet. *J. Phys. Condens. Matter* **2015**, *27*, 496001. [CrossRef] [PubMed]
32. Costantini, J.-M.; Miro, S.; Lelong, G.; Guillaumet, M.; Toulemonde, M. Damage Induced in Garnets by Heavy-Ion Irradiations: A Study by Optical Spectroscopies. *Philos. Mag.* **2018**, *98*, 312–328. [CrossRef]
33. Thomé, L. Swift Heavy Ion Irradiation of Crystalline Insulators and Metals. In *Ion Beam Modification of Solids*; Springer Series in Surface Sciences; Springer: Cham, Switzerland, 2016; Volume 61, pp. 321–363. [CrossRef]
34. Izerrouken, M.; Bucher, R.; Meftah, A.; Maaza, M. XRD and AFM Study of Radiation Damage Induced by Swift Heavy Ions in $Y_3Al_5O_{12}$ Single Crystals. *Radiat. Eff. Defects Solids* **2011**, *166*, 513–521. [CrossRef]
35. Meftah, A.; Benhacine, H.; Benyagoub, A.; Grob, J.J.; Izerrouken, M.; Kadid, S.; Khalfaoui, N.; Stoquert, J.P.; Toulemonde, M.; Trautmann, C. Data Consistencies of Swift Heavy Ion Induced Damage Creation in $Y_3Fe_5O_{12}$. *Nucl. Instrum. Methods Phys. Res. B* **2016**, *366*, 155–160. [CrossRef]
36. Matkovskii, A.; Sugak, D.; Melnyk, S.; Potera, P.; Suchocki, A.; Frukacz, Z. Colour Centers in Doped $Gd_3Ga_5O_{12}$ and $Y_3Al_5O_{12}$ Laser Crystals. *J. Alloys Compd.* **2000**, *300–301*, 395–397. [CrossRef]

37. Kozlovskiy, A.L.; Konuhova, M.; Shlimas, D.I.; Borgekov, D.B.; Zdorovets, M.V.; Shakirziyanov, R.I.; Popov, A.I. Study of the Effect of Nanostructured Grains on the Radiation Resistance of Zirconium Dioxide Ceramics During Gas Swelling under High-Dose Irradiation with Helium Ions. *ES Mater. Manuf.* **2024**, *24*, 1165. [CrossRef]
38. Kozlovskiy, A.L.; Konuhova, M.; Borgekov, D.B.; Popov, A.I. Study of Irradiation Temperature Effect on Radiation-Induced Polymorphic Transformation Mechanisms in ZrO_2 Ceramics. *Opt. Mater.* **2024**, *156*, 115994. [CrossRef]
39. Zdorovets, M.V.; Kozlovskiy, A.A.; Moldabayeva, G.Z.; Ivanov, I.A.; Konuhova, M. Radiation-Induced Degradation Effects of Optical Properties of MgO Ceramics Caused by Heavy Ion Irradiation. *Opt. Mater. X* **2025**, *26*, 100406. [CrossRef]
40. Ryskulov, A.E.; Ivanov, I.A.; Kozlovskiy, A.L.; Konuhova, M. The Effect of Residual Mechanical Stresses and Vacancy Defects on the Diffusion Expansion of the Damaged Layer During Irradiation of BeO Ceramics. *Opt. Mater. X* **2024**, *24*, 100375. [CrossRef]
41. Malikova, Z.; Karipbayev, Z.T.; Akilbekov, A.; Dauletbekova, A.; Popov, A.I.; Kuzovkov, V.N.; Abdrakhmetova, A.; Russakova, A.; Baizhumanov, M. Thermal Stability of Color Centers in Lithium Fluoride Crystals Irradiated with Electrons and N, O, Kr, U Ions. *Materials* **2025**, *18*, 4441. [CrossRef]
42. Manika, I.; Krasta, T.; Maniks, J.; Bikse, L.; Susinska, J.; Leimane, M.; Trausa, A.; Grants, R.; Popov, A.I. Effect of Ion Irradiation on Structure Modification and Radiolysis in LiF Crystals Irradiated by 410 MeV ^{36}S Ions. *Opt. Mater.* **2023**, *138*, 113686. [CrossRef]
43. Popov, A.I.; Elsts, E.; Kotomin, E.A.; Moskina, A.; Karipbayev, Z.T.; Makarenko, I.; Pazylbek, S.; Kuzovkov, V.K. Thermal Annealing of Radiation Defects in MgF_2 Single Crystals Induced by Neutrons at Low Temperatures. *Nucl. Instrum. Methods Phys. Res. Sect. B* **2020**, *480*, 16–21. [CrossRef]
44. Bhandari, K.; Grover, V.; Kalita, P.; Sudarshan, K.; Modak, B.; Sharma, S.K.; Kulriya, P.K. Radiation Response of $Y_3Al_5O_{12}$ and Nd^{3+}-$Y_3Al_5O_{12}$ to Swift Heavy Ions: Insight into Structural Damage and Defect Dynamics. *Phys. Chem. Chem. Phys.* **2023**, *25*, 20495–20509. [CrossRef]
45. Costantini, J.M.; Desvignes, J.M.; Toulemonde, M. Amorphization and Recrystallization of Yttrium Iron Garnet under Swift Heavy Ion Beams. *J. Appl. Phys.* **2000**, *87*, 4164–4174. [CrossRef]
46. Costantini, J.M.; Desvignes, J.M.; Pérez, A.; Studer, F. Local Order and Magnetic Behavior of Amorphous and Nanocrystalline Yttrium Iron Garnet Produced by Swift Heavy Ion Irradiations. *J. Appl. Phys.* **2000**, *87*, 1899–1907. [CrossRef]
47. Izerrouken, M.; Khereddine, A.; Sari, A.; Meftah, A. Mechanical Properties of Swift Heavy Ion Irradiated $Y_3Al_5O_{12}$ Single Crystal. *Nucl. Instrum. Methods Phys. Res. Sect. B* **2018**, *435*, 137–141. [CrossRef]
48. Nazarov, A.A.; Yunin, P.A.; Alekseeva, L.S.; Nokhrin, A.V. X-ray Diffraction Study and Modeling of Damaged Layers in $Y_{2.5}Nd_{0.5}Al_5O_{12}$ Ceramics after Swift Heavy Xe Ion Irradiation. *Phys. Part. Nucl. Lett.* **2025**, *22*, 1094–1098. [CrossRef]
49. Szenes, G.; Pászti, F.; Péter, Á.; Popov, A.I. Tracks Induced in TeO_2 by Heavy Ions at Low Velocities. *Nucl. Instrum. Methods Phys. Res. B* **2000**, *166*, 949–953. [CrossRef]
50. Szenes, G. Uniform Behavior of Insulators Irradiated by Swift Heavy Ions. *Nucl. Instrum. Methods Phys. Res. B* **2015**, *354*, 47–50. [CrossRef]
51. Karlušić, M.; Ghica, C.; Negrea, R.F.; Siketić, Z.; Jakšić, M.; Schleberger, M.; Fazinić, S. On the threshold for ion track formation in CaF_2. *New J. Phys.* **2017**, *19*, 023023. [CrossRef]
52. Karlušić, M.; Jakšić, M.; Lebius, H.; Ban-d'Etat, B.; Wilhelm, R.A.; Heller, R.; Schleberger, M. Swift heavy ion track formation in $SrTiO_3$ and TiO_2 under randon, channeling and near-channeling conditions. *J. Phys. D Appl. Phys.* **2017**, *50*, 205302. [CrossRef]
53. Fodchuk, I.; Kotsyubynsky, A.; Velychkovych, A.; Hutsuliak, I.; Boychuk, V.; Kotsyubynsky, V.; Ropyak, L. The Effect of Ne^+ Ion Implantation on the Crystal, Magnetic, and Domain Structures of Yttrium Iron Garnet Films. *Crystals* **2022**, *12*, 1485. [CrossRef]
54. Giniyatova, S.G.; Kozlovskiy, A.L.; Rspayev, R.M.; Borgekov, D.B.; Zdorovets, M.V. Study of the Kinetics of Radiation Damage in CeO_2 Ceramics upon Irradiation with Heavy Ions. *Materials* **2023**, *16*, 4653. [CrossRef] [PubMed]
55. Kotomin, E.A.; Kashcheyevs, V.; Kuzovkov, V.N.; Schwartz, K.; Trautmann, C. Modeling of Primary Defect Aggregation in Tracks of Swift Heavy Ions in LiF. *Phys. Rev. B* **2001**, *64*, 144108. [CrossRef]
56. Davidson, A.T.; Schwartz, K.; Comins, J.D.; Kozakiewicz, A.G.; Toulemonde, M.; Trautmann, C. Vacuum Ultraviolet Absorption and Ion Track Effects in LiF Crystals Irradiated with Swift Ions. *Phys. Rev. B* **2002**, *66*, 214102. [CrossRef]
57. Aumayr, F.; Facsko, S.; El-Said, A.S.; Trautmann, C.; Schleberger, M. Single Ion Induced Surface nanostructures: A Comparison between Slow Highly Charged and Swift Heavy Ions. *J. Phys. Condens. Matter* **2011**, *23*, 393001. [CrossRef] [PubMed]
58. Amekura, H.; Ishikawa, N.; Okubo, N.; Chen, F.; Narumi, K.; Chiba, A.; Hirano, Y.; Yamada, K.; Yamamoto, S.; Saitoh, Y. Metallic Ca Aggregates Formed Along Ion Tracks and Optical Anisotropy in CaF_2 Crystals Irradiated with Swift Heavy Ions. *Quantum Beam Sci.* **2024**, *8*, 29. [CrossRef]
59. Itoh, N.; Duffy, D.M.; Khakshouri, S.; Stoneham, A.M. Making tracks: Electronic excitation roles in forming swift heavy ion tracks. *J. Phys. Condens. Matter* **2009**, *21*, 474205. [CrossRef]
60. Takaki, S.; Yasuda, K.; Yamamoto, T.; Matsumura, S.; Ishikawa, N. Structure of Ion Tracks in Ceria Irradiated with High Energy Xenon Ions. *Prog. Nucl. Energy* **2016**, *92*, 306–312. [CrossRef]
61. Ishikawa, N.; Fukuda, S.; Nakajima, T.; Ogawa, H.; Fujimura, Y.; Taguchi, T. Ion Tracks and Nanohillocks Created in Natural Zirconia Irradiated with Swift Heavy Ions. *Materials* **2024**, *17*, 547. [CrossRef]

62. Hu, P.P.; Liu, J.; Zhang, S.X.; Maaz, K.; Zeng, J.; Guo, H.; Hou, M.D. Raman Investigation of Lattice Defects and Stress Induced in InP and GaN Films by Swift Heavy Ion Irradiation. *Nucl. Instrum. Methods Phys. Res. B* **2016**, *372*, 29–37. [CrossRef]
63. Costantini, J.M.; Gutierrez, G.; Lelong, G.; Guillaumet, M.; Rahman, M.M.; Yasuda, K. Raman Spectroscopy Study of Damage in Swift Heavy Ion-Irradiated Ceramics. *J. Raman Spectrosc.* **2022**, *53*, 1614–1624. [CrossRef]
64. Tunhuma, S.M.; Diale, M.; Nel, J.M.; Madito, M.J.; Hlatshwayo, T.T.; Auret, F.D. Defects in Swift Heavy Ion Irradiated n-4H-SiC. *Nucl. Instrum. Methods Phys. Res. B* **2019**, *460*, 119–124. [CrossRef]
65. Song, Y.; Zhang, S.; Zhang, C.; Yang, Y.; Lv, K. Raman Spectra and Microstructure of Zinc Oxide Irradiated with Swift Heavy Ions. *Crystals* **2019**, *9*, 395. [CrossRef]
66. Guo, H.; Sun, Y.; Zhai, P.; Zeng, J.; Zhang, S.; Hu, P.; Yao, H.; Duan, J.; Hou, M.; Liu, J. Resonant Raman Spectroscopy Study of Swift Heavy Ion Irradiated MoS_2. *Nucl. Instrum. Methods Phys. Res. B* **2016**, *381*, 1–5. [CrossRef]
67. Costantini, J.M.; Miro, S.; Gutierrez, G.; Yasuda, K.; Takaki, S.; Ishikawa, N.; Toulemonde, M. Raman Spectroscopy Study of Damage Induced in Cerium Dioxide by Swift Heavy Ion Irradiations. *J. Appl. Phys.* **2017**, *122*, 203104. [CrossRef]
68. Khatter, J.; Panchal, S.; Chauhan, R.P. Swift Heavy Ion Irradiation Induced Modifications in Electron Beam Deposited CdS Thin Films. *J. Alloys Compd.* **2022**, *924*, 166641. [CrossRef]
69. Platonenko, A.; Gryaznov, D.; Popov, A.I.; Dovesi, R.; Kotomin, E.A. First principles calculations of the vibrational properties of single and dimer F-type centers in corundum crystals. *J. Chem. Phys.* **2020**, *153*, 134107. [CrossRef]
70. Akilbekov, A.; Kenbayev, D.; Dauletbekova, A.; Polisadova, E.; Yakovlev, V.; Karipbayev, Z.; Shalaev, A.; Elsts, E.; Popov, A.I. The Effect of Fast Kr Ion Irradiation on the Optical Absorption, Luminescence, and Raman Spectra of BaFBr Crystals. *Crystals* **2023**, *13*, 1260. [CrossRef]
71. Khomich, A.A.; Khmelnitsky, R.A.; Khomich, A.V. Probing the nanostructure of neutron-irradiated diamond using Raman spectroscopy. *Nanomaterials* **2020**, *10*, 1166. [CrossRef] [PubMed]